AIAA JOURNAL
Vol. 45, No. 10, October 2007

Large-Eddy-Simulation Modeling for Aerothermal Predictions Behind a Jet in Crossflow

J-C. Jouhaud,* L. Y. M. Gicquel,* and B. Enaux†
CERFACS, 31057 Toulouse, France
and
M-J. Esteve‡
Airbus France, 31060 Toulouse, France

DOI: 10.2514/1.28392

Numerical investigations of a hot square jet in crossflow issuing perpendicularly to a flat plate are presented. This current work is initiated by Airbus Industries to better predict the aircraft aerothermal environment. Advanced numerical methods are tested in this specific context. In particular, the numerical approaches of large eddy simulations and Reynolds-averaged Navier–Stokes simulations are assessed in an industrylike configuration. Specific attention is brought to the large eddy simulations of a jet in a crossflow momentum-flux ratio of 0.77 and a Reynolds number of 93,900 (based on crossflow velocity and jet diameter). Numerical issues such as grid resolution and boundary condition choices are addressed. Comparison of the Reynolds-averaged quantities obtained from large eddy simulations with Reynolds-averaged Navier–Stokes simulation data at several cross-stream locations underlines the potential of large eddy simulations for aerothermal predictions. Large-scale motions observed experimentally and numerically are reproduced by the unsteady large-eddy-simulation fields, and spectral analyses reveal the ability of the large eddy simulations to reproduce the coherent structure frequencies.

Introduction

THIS work stems from the aerothermal flow modeling in aircraft ventilation (MAEVA) project directed by Airbus France and ONERA with the cooperation of CERFACS. The aim of this project is to enhance the understanding and the prediction of the aircraft's thermal environment to deal with the problems of composite materials. Indeed, for an identical mass, these materials are more resistant than the materials they replace. However, they are also more sensitive to the temperature variations and may age prematurely under extreme conditions. The MAEVA project is organized around three classes of problems: 1) the impact of a hot jet on a cold wall, 2) the mixed convection problem appearing in cavities, and 3) the interaction of a hot jet in crossflow (JICF) with a cold wall.

The purpose of this study is to assess large eddy simulation (LES) for the third class of problems. Contrary to the Reynolds-averaged Navier–Stokes (RANS) simulation technique, which is restricted to steady turbulent flows, LES takes into account flow instabilities by solving for large flow structures while modeling the small-scale effects. The implications of the numerical predictions are of importance, but still need to be illustrated and validated in the context of the industrial applications in which thermal effects are of interest.

The investigation presented in this document aims at the modeling of the interaction between a hot JICF (see Margason [1] for a detailed review on JICFs and their applications) and the wall of a turbofan engine nacelle. The interaction takes place on the leading edge of the nacelle, on which hot air is injected through the wall of the nacelle to avoid icing on the exterior (see Fig. 1). The hot air is collected in a scoop and ejected on the leading edge of the nacelle to form the JICF. Because the velocities are on the order of tens of $m \cdot s^{-1}$, temperature can be considered as a passive scalar.

The objective of engine designers is to determine the essential characteristics of the jet and its development, but not to simulate the flow around the turbofan engine. The jet is thus studied in the simplified geometry of the flat-plate configuration. This choice is justified by the fact that the nacelle has relatively low curvature and the jet diameter is very small in comparison with the dimension of the turbofan engine. The zone in which the jet mixes with the crossflow can then be regarded as quasi planar. Experimental data to be used in the validation of the numerical methods for this industrylike configuration were obtained using an apparatus located at ONERA. Velocity fields within the flow domain and thermal fields on the plate can be used to assess LES. The specific effect of the grid resolution on the LES predictions is also tested by performing computations on two meshes: a coarse grid and a fine grid.

This paper starts with a detailed presentation of the flow topology observed in free JICF. This is followed by a description of the LES methodology and a presentation of the computational domain. LES predictions are then compared with RANS predictions [2] and experimental measures. The results are then discussed with a detailed description of the mechanisms by which LES provides superior predictions to RANS in this aerothermal problem. To further analyze these encouraging results, coherent structures are investigated and spectral analyses are performed on the velocity signal obtained by LES.

Flow Physics of a Jet in Crossflow

Flow Features

The JICF configurations have been studied for many years because of their wide use in applications such as V/STOL aircraft in transition flight, turbine film cooling, chimneys, roll control for rockets, or fuel mixing in the combustion chamber [3,4].

The JICF is a flow configuration that allows rapid mixing of two fluids, due to complex three-dimensional interactions. The results of these interactions between the jet and the transverse flow are coherent structures that were identified in the seventies [5,6]. Nowadays, numerous investigations of these structures have been undertaken and they agree on four principal vortices (see Fig. 2):

1) The counter-rotating vortex pair (CVP) is the dominant structure of the flow configuration far downstream of the jet orifice. It

Received 17 October 2006; revision received 25 May 2007; accepted for publication 4 June 2007.

*Senior Researcher, Computational Fluid Dynamics Team, 42 Avenue Gaspard Coriolis.
†Ph.D. Student, Computational Fluid Dynamics Team, 42 Avenue Gaspard Coriolis.
‡Research Engineer, 316 Route de Bayonne.

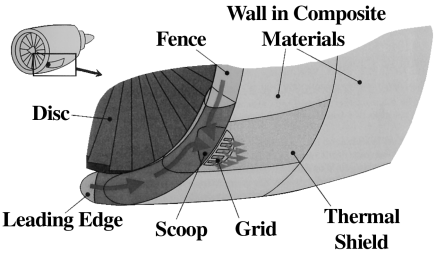

Fig. 1 Schematic illustration of the engine anti-icing system.

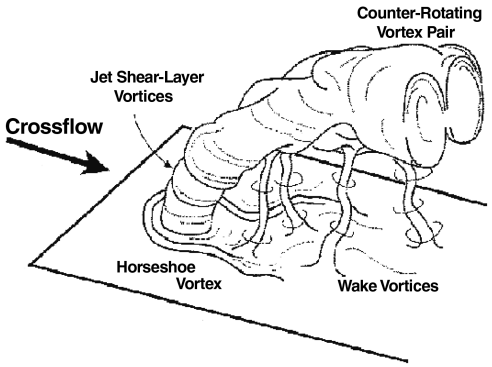

Fig. 2 Schematic illustration of the vortex system in a JICF [16].

is formed by the deflection of the jet and is convected by the transverse flow. Experimental studies show that the CVP evolves from the reorientation of the shear-layer vortices of the jet [7–10]. This mechanism is confirmed by the numerical investigation of Cortelezzi and Karagozian [11]. It is also important to notice that this is the main flow structure responsible for most of the mixing between the two fluids.

2) The horseshoe vortex is due to the adverse pressure gradient generated at the wall just ahead of the jet. This structure is quite similar to the structure observed for flows around a solid cylinder, and Krothapalli et al. [12] observed that the vortex-shedding frequency is quite similar to that around a solid cylinder ($St = fD/U_0 = 0.21$, where D is the cylinder diameter, U_0 is the stream velocity, and f is the shedding frequency).

3) Shear-layer ring vortices evolve on the jet circumference and are generated in the boundary layer of the jet orifice. These vortices become distorted when the jet is deflected, and the mechanism of the shear-layer evolution is interpreted by Kelso et al. [13]. The shear generated when the two streams meet (crossflow and jet streams) creates a Kelvin–Helmholtz instability, causing the flow to roll up around the jet's circumference. This rollup creates vortex tubes that extend up and around the jet and that eventually shed into the main flow. These structures are named "hanging vortices" by Yuan et al. [14].

4) Wake vortices have been studied experimentally [7,15,16], but are the least understood. However, the experiments of Fric and Roshko [16] suggested that this vorticity originates from the wall boundary layer, in which the boundary layer wraps around the jet. These flow patterns seem to be influenced by the jet trajectory.

Correlations Parameters

A JICF can be characterized by mean quantity ratios involving velocity and density. The first parameter is the velocity ratio:

$$V_R = \frac{U_{\text{jet}}}{U_{\text{cross}}} \tag{1}$$

where U_{jet} is the jet bulk velocity, and U_{cross} is the cross-stream velocity.

If the density of the jet is different from the density of the crossflow, the velocity ratio Eq. (1) no longer describes the jet centerline evolution. The following parameter [17] is thus preferred:

$$C_R = \frac{\rho_j U_{\text{jet}}}{\rho_0 U_{\text{cross}}} \tag{2}$$

The next parameter shows better parameterization properties [18] in the case of significant thermal variations and is the square root of the momentum-flux ratio:

$$R = \sqrt{\frac{\rho_j U_{\text{jet}}^2}{\rho_0 U_{\text{cross}}^2}} \tag{3}$$

In the present case, $C_R = 0.7$ and $R = 0.9$. For these low values, the jet is expected to remain within the crossflow boundary layer. Such jet velocity ratios ($C_R < 1$) have been studied experimentally [19] and numerically [20] on a round JICF. However, no published data on such jet velocity ratios deal with a square JICF. Renze et al. [20] studied the impact of the density ratio on angled jets, and Andreopoulos [19] investigated a jet issuing perpendicularly but with a density ratio equal to unity.

Numerical Simulation: LES

The aim of the LES is to resolve the large scale of turbulence, and the smaller ones are modeled based on their universality. In contrast, RANS attempts to model all of the flow scales at once. Consequently, LES are better suited to industrial configurations, in which large scales are known to be essential. In the case of the JICF, in which the unsteady behavior of the various flow structures is expected to be important, the unsteady LES approach that provides spatiotemporal resolution should be used.

Governing Equations

A filtering operation is applied to the continuity equation, the momentum equation, and the total energy equation. In the case of compressible flows, a Favre filtering [21] is used:

$$\bar{\rho}\,\tilde{f}(\mathbf{x},t) = \overline{\rho f(\mathbf{x},t)} = \int_{-\infty}^{+\infty} \rho f(\mathbf{x}',t)\mathcal{G}(\mathbf{x}'-\mathbf{x})\,\mathrm{d}\mathbf{x}' \tag{4}$$

where $\mathcal{G}$ is the filter function, ρ is the density, and f can be either the velocity vector, the total energy, or the mass fraction of species. The application of the filtering operation to the set of governing compressible Navier–Stokes equations yields [22–24]

$$\begin{aligned}
&\frac{\partial \bar{\rho}}{\partial t} + \frac{\partial}{\partial x_j}(\bar{\rho}\tilde{u}_j) = 0\\
&\frac{\partial \bar{\rho}\tilde{u}_i}{\partial t} + \frac{\partial}{\partial x_j}(\bar{\rho}\tilde{u}_i\tilde{u}_j) = -\frac{\partial}{\partial x_j}[\bar{P}\delta_{ij} - \bar{\tau}_{ij} - \bar{\tau}^t_{ij}]\\
&\frac{\partial \bar{\rho}\tilde{E}}{\partial t} + \frac{\partial}{\partial x_j}(\bar{\rho}\tilde{E}\,\tilde{u}_j) = -\frac{\partial}{\partial x_j}[\overline{u_i(P\delta_{ij} - \tau_{ij})} + \bar{q}_j + \bar{q}^t_j]
\end{aligned} \tag{5}$$

where

$$\begin{aligned}
\bar{\tau}_{ij} &= \overline{2\mu\left(S_{ij} - \tfrac{1}{3}\delta_{ij}S_{kk}\right)}\\
&\approx 2\bar{\mu}\left(\tilde{S}_{ij} - \tfrac{1}{3}\delta_{ij}\tilde{S}_{kk}\right)\\
\bar{q}_i &= -\overline{\lambda\frac{\partial T}{\partial x_i}}\\
&\approx -\bar{\lambda}\frac{\partial \tilde{T}}{\partial x_i}
\end{aligned} \tag{6}$$

and

$$\tilde{S}_{ij} = \frac{1}{2}\left(\frac{\partial \tilde{u}_j}{\partial x_i} + \frac{\partial \tilde{u}_j}{\partial x_j}\right) \tag{7}$$

This set of partial differential equations is supplemented by the ideal gas law $\bar{P} = \bar{\rho}\widetilde{rT}$, where r is the gas constant.

Subgrid-Scale Model

In Eq. (5), the terms $\bar{\tau}^t_{ij}$ and $\bar{q}^t_j$ need to be modeled to close the set of LES equations. To do so, the Boussinesq hypothesis (8) is introduced to mimic the subgrid-scale action on the resolved field:

$$\bar{\tau}^{\,t}_{ij} = -\bar{\rho}(\widetilde{u_i u_j} - \tilde{u}_i\tilde{u}_j) = 2\bar{\rho}\nu_t(\tilde{S}_{ij} - \tfrac{1}{3}\tilde{S}_{kk}\delta_{ij}) + \tfrac{1}{3}\bar{\tau}^t_{kk}\delta_{ij} \quad (8)$$

where the subgrid-scale turbulent viscosity ν_t needs to be given. Here, the standard Smagorinsky [25] model is used:

$$\nu_t = (C_S\triangle)^2\sqrt{2\tilde{S}_{ij}\tilde{S}_{ij}} \quad (9)$$

where $\triangle$ denotes the filter characteristic length (cube root of the cell volume), and C_S is the standard model constant set to 0.18. Finally, the thermal turbulent heat flux $\bar{\rho}^t_j$ is closed through the use of the turbulent Prandtl number $Pr_t = 0.9$, along with a gradient hypothesis.

Flow Solver

In the present work, the fully compressible LES equations are solved on unstructured grids composed of tetrahedral cells in a code called AVBP [26]. For this code, the subgrid-scale turbulence is modeled with the Smagorinsky model and with wall functions [27]. The numerical implementation is based on the classical centered finite volume cell-vertex space discretization of Lax–Wendroff. For time integration, the explicit four-stage Runge–Kutta scheme is used with CFL = 0.7.

Flow Domain

As illustrated in Fig. 3, hot air is injected into tubes (inlets 1 and 2) that reach a settling chamber called a scoop. The scoop is covered on the top by a fine copper plate denoted by a grid. The hot air mixes in the scoop and is ejected vertically into the cold cross stream that flows over the flat plate. The width of the injection orifice D measures 30 mm, and the jet exit is flush with the horizontal flat plate.

The jet orifice is located $X/D = 2.8$ downstream of the domain inlet and $X/D = 33.3$ upstream of the outlet. Each lateral face of the computational domain is located $Y/D = 27.8$ from the jet orifice, and the domain size used for the computation is $37.2 \times 46.5\times 33.3D$. The spreading of the jet is not restricted by the domain.

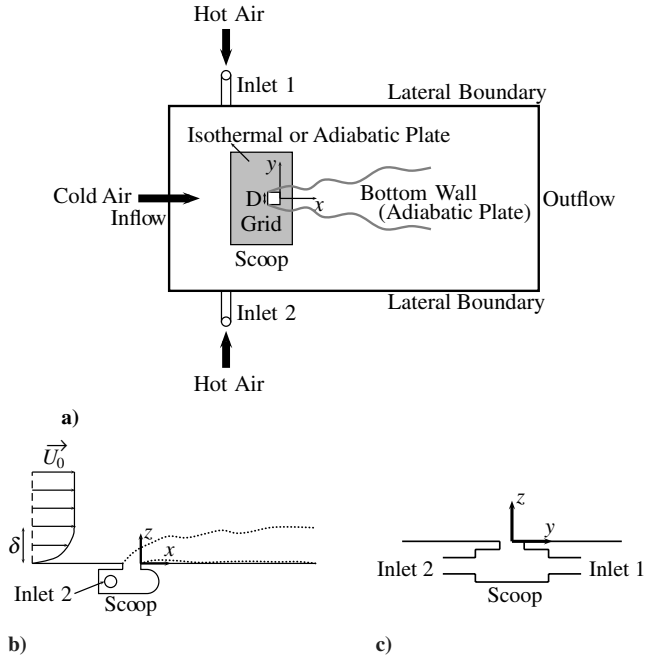

Fig. 3 Computational domain considered for LES: a) top view, b) lateral view, and c) front view.

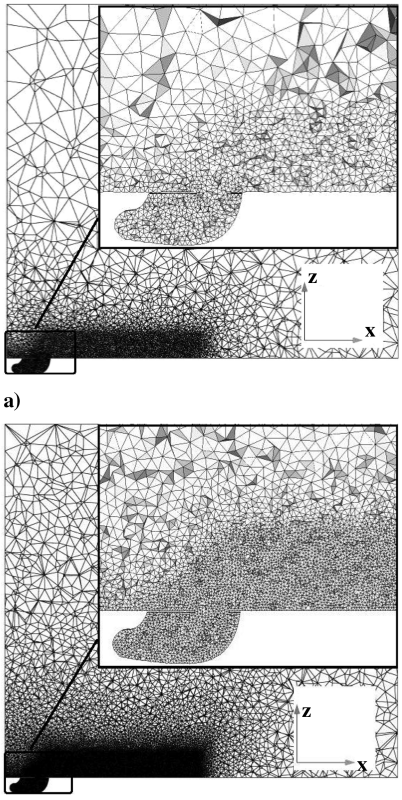

Fig. 4 Cross view of the mesh refinement in the $Y/D = 0$ plane: a) the coarse mesh M_1, and b) the fine mesh M_2.

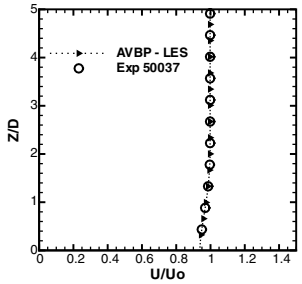

Fig. 5 Velocity profile imposed in the main inlet ($X/D = -4.0$, coarsest mesh).

Two grids (Fig. 4) are used for the simulation: a coarse mesh M_1 containing 580,000 cells and a finer mesh M_2 composed of 2.74×10^6 cells. Each unstructured mesh is composed of tetrahedral cells, and grid refinement is enforced along the jet trajectory and in the near-wall region. $M1$ and $M2$ have the same topology and they only differ in their mesh density (locally, the finest mesh is two times more refined) in the region of the JICF interaction and inside the scoop (see the insets in Fig. 4). There are around 150 points ($\Delta x \approx \Delta y \approx$ 0.2 mm) and 300 points ($\Delta x \approx \Delta y \approx 0.1$ mm) in the square-jet orifice, for the coarse mesh and the fine mesh, respectively. These two computational grids follow the approach used for similar flows [28,29] and they permit a good representation of the interaction.

The flow to be simulated corresponds to the MAEVA [2] experimental test case (modelization of aerothermal flows for aircraft ventilation). It is characterized by a crossflow Reynolds number of 93,900 (based on the injection hydraulic diameter D). The boundary-layer thickness of the flat plate seen by the crossflow is $\delta/D = 0.13$. To allow a manageable number of cells, a law-of-the-wall model is

used at the bottom surface. In both grids, the cells adjacent to the bottom wall have sizes corresponding to Δx^+, Δy^+, and $\Delta z^+ \gg 1$ ($\Delta x^+ = 110$, $\Delta y^+ = 150$, $\Delta z^+ = 130$ for M_2, $\Delta x^+ = 420$, $\Delta y^+ = 450$, and $\Delta z^+ = 460$ for M_1). Use of a law of the wall is justified here because $\delta/D = 0.13$: the inlet turbulence is one order of magnitude under the turbulence generated by the jet.

Boundary Conditions

In accordance with the experimental measurements, the flow through the main inlet is imposed by using a velocity profile that includes a boundary layer at the wall. The profile was chosen to exactly match the experimental profile (see Fig. 5), including the log-layer region. In this way, we expect to simulate the correct boundary-layer thickness before the jet interaction.

The initial boundary-layer height is $2D$ and the freestream velocity is $U_0 = 47.1\ \text{m} \cdot \text{s}^{-1}$. The injection pipes that feed into the scoop are given mean turbulent pipe profiles according to the standard one-seventh power-law approximation (Table 1). All of these velocity profiles agree with the mass flux of the experiments and the temperature conditions. Because of the acoustic waves present in LES and inherent to the compressible flow solver, characteristic boundary conditions [30,31] are applied at all inlets, with relaxation coefficients [32] of the velocity, the temperature, and the mass fraction of the species. The same type of characteristic boundary condition is applied at the outlet, but only pressure is specified. The bottom plate is divided in two parts. The grid region immediately surrounding the jet orifice uses either a no-slip isothermal-wall-law condition (M_2) or a no-slip adiabatic-wall-law condition (M_1 and M_2). The remaining area of the plate is treated by use of a no-slip adiabatic-wall-law condition. At the lateral boundaries, symmetry conditions are enforced, and a slip adiabatic-wall condition is imposed on the top surface of the computational domain. The latter condition is valid in our case, because it is located sufficiently far from the jet exhaust ($33.3D$ above the plate). All of the boundary conditions used for LES are summarized in Table 2.

Results

Comparison with Experiment and RANS Predictions

In this section, a comparison is made between the flowfield results of the experiment, RANS, and LES. The experimental measurements [2] are obtained using particle image velocimetry (experiment 50,036) and laser Doppler anemometry (experiment 50,037) on several cross-stream sections perpendicular to the jet. In addition to this database, hot-wire measurements (experiment 11,300) are provided for the heated jet in the form of temperature maps.

Table 1 Set of reference values applied at the boundary conditions of LES

Boundary name	Velocity, $\text{m} \cdot \text{s}^{-1}$	Temperature, K	Pressure, Pa
Inlet1	$\lvert V_1 \rvert = 53.1$	$T_1 = 363$	$P_1 = 98,701$
Inlet2	$\lvert V_2 \rvert = 53.1$	$T_2 = 363$	$P_2 = 98,701$
Inflow	$U_0 = 47.1$	$T_0 = 293$	$P_0 = 98,701$

Table 2 Boundary condition specification

Boundary name	Fixed quantities	Relaxation coefficient
Inlet1	U, V, W, T, Y	$\sigma_{U,V,W,T,Y} = 50$
Inlet2	U, V, W, T, Y	$\sigma_{U,V,W,T,Y} = 50$
Inflow	U, V, W, T, Y	$\sigma_{U,V,W,T,Y} = 50$
Outflow	P	$\sigma_P = 50$
	T	
	$q_{\text{wall}} = 0$	NA
Scoop	$q_{\text{wall}} = 0$	NA
Bottom wall	$q_{\text{wall}} = 0$	NA
Lateral surfaces	Symmetry	NA
Top surface	$q_{\text{wall}} = 0$	NA

The RANS calculation was performed with the elsA[33] code of Airbus. The characteristics of the simulation are 1) a structured mesh composed of 5.9×10^6 cells, with the first cell adjacent to the bottom wall corresponding to $\Delta y^+ \approx 1$; 2) the $k-l$ two-equation turbulence model of Smith and Mungal [15]; 3) a cell-centered finite volume method; and 4) an implicit method for time integration with a Courant–Friedrichs–Lewy number equal to 3000.

All of the results obtained by LES are time-averaged to be directly comparable to the RANS and experimental data. Time integration in this case is carried out over a duration equal to 2.5 flow-through times, with a flow-through time being obtained based on the cross-stream bulk velocity and the computational length (i.e., $47.1\ \text{m} \cdot \text{s}^{-1}$ and $37.2D$). This duration is sufficient for convergence of all average quantities.

The predictions are assessed on velocity and kinetic energy profiles at three cross planes located at $X/D = 1$, 3, and 8 downstream of the jet exit. Furthermore, comparison of the cooling effectiveness η allows an assessment of the potential for each approach to predict the thermal process and the mixing behavior. In the following, the cooling effectiveness is defined by

$$\eta = \frac{\langle T_w \rangle - T_0}{T_j - T_0} \tag{10}$$

where $\langle T_w \rangle$ is the temporally averaged local wall temperature, T_j is the jet temperature, and T_0 is the temperature of the crossflow upstream of the jet exit. Profiles of η are presented for different streamwise locations ($X/D = 1$, 8, 14), and one more profile is plotted in the spanwise symmetry plane ($Y/D = 0$).

The effect of the boundary condition to be applied at the grid is also addressed in terms of η profiles. Indeed, the exact thermal boundary condition to be used in this wall region is not clear, because of the composition of the grid: 1-mm-thick copper plate. To investigate its importance, two simulations are carried out using mesh M_2 only: one LES in which the grid is considered as adiabatic and a second LES in which the grid is considered as isothermal, with a grid temperature approximated as the average temperature between the two grid sides. The following section illustrates the importance of this boundary condition for the proper prediction of the cooling effectiveness.

Coarse-Grid Results. In this simulation, the grid is considered as adiabatic. An instantaneous visualization of the temperature field (Fig. 6) shows that the cells are too coarse to properly represent the coherent structures located in the shear layer. However, velocity profiles presented in Fig. 7 show a rather good correspondence between LES/RANS/experiments, except perhaps at the cross plane $X/D = 1$. In fact, the measured reverse flow is not well-predicted by either simulation. This backflow is not captured, because of the wall grid resolution and modeling of LES, which seems inadequate.

With regard to the prediction of mixing, the cooling-effectiveness profiles predicted by LES in Fig. 8 are underestimated whether they are in the streamwise locations or in the spanwise symmetry plane.

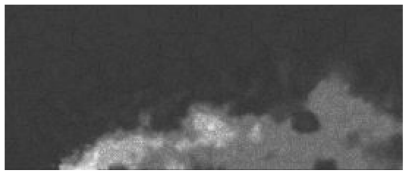

a)

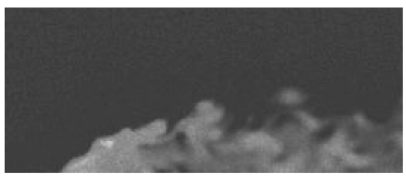

b)

Fig. 6 Instantaneous view of temperature (white is hold and black is cold) as obtained by LES in the $Y/D = 0$ plane: a) Coarse mesh M_1, and b) Fine mesh M_2.

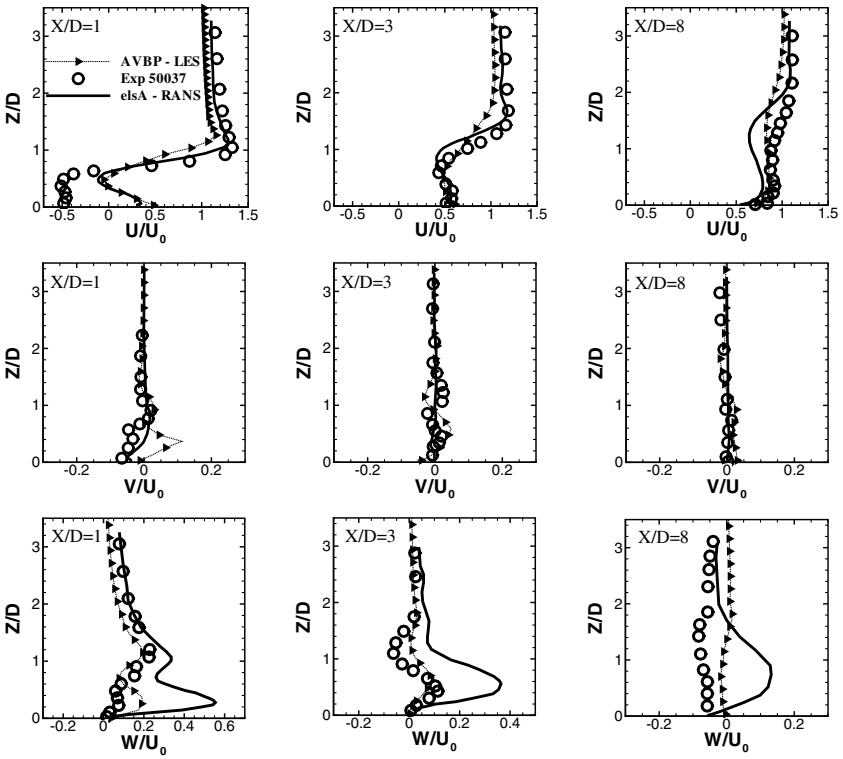

Fig. 7 Comparison of the velocity profiles in the symmetry plane at different streamwise locations (simulation on mesh M_1).

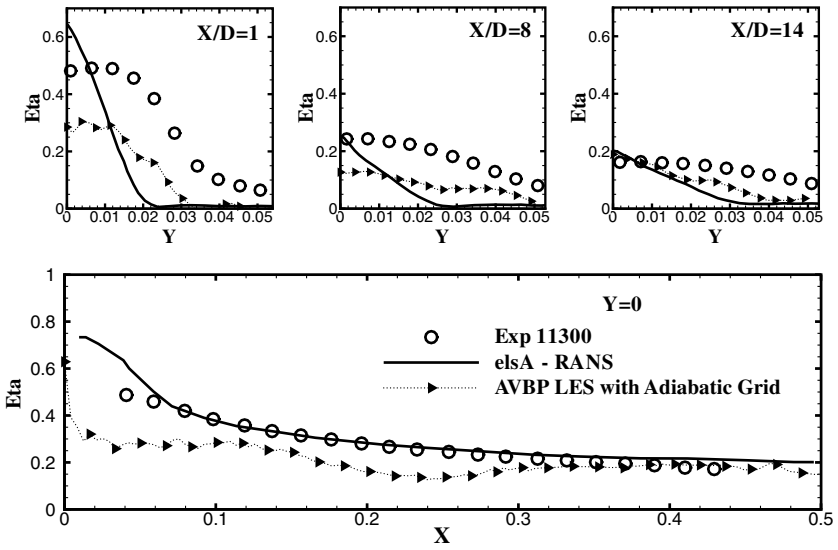

Fig. 8 Comparison of the wall-cooling-effectiveness profiles at different streamwise locations and in the spanwise symmetry plane ($Y = 0$) (simulation on mesh M_1).

The underestimation of the mixing behavior is also evidenced by the velocity field comparison (Fig. 9). The vertical-velocity vector component V/U_0 shows that the CVP predicted by LES is not as strong as it should be. The field U/U_0 also shows that the jet penetration is not well-reproduced. LES tends to overestimate the jet penetration, which can partly be explained by incorrect jet/wall interaction caused by the poor grid resolution in the near-wall region.

Fine-Grid Results. To assess the effect of mesh refinement along the jet trajectory, a new simulation is conducted based on mesh M_2. The first LES used a no-slip adiabatic-wall-law condition and the second LES used a no-slip isothermal-wall-law condition on the grid.

The comparison between LES predictions and measured data shows very good agreement and clearly illustrates the impact of the grid resolution on the LES predictions (Fig. 6). Because of refinement, definite structures are observed that are not dissipated excessively, resulting in enhanced prediction of the mixing process. The velocity field V/U_0 illustrated in Fig. 10 shows that the intensity of the CVP is well-predicted. Similarly, the jet penetration is improved when compared with the mesh M_1 predictions, and the M_2 results better reproduce the experimental observations.

The fine-grid LES captures more coherent structures of the JICF, which should directly impact the predictions of cooling effectiveness (Fig. 11). The η profile in the spanwise symmetry plane of Fig. 11 is well-predicted and RANS or LES equally well-reproduce the experimental measurements. Given the length of the thermal trace, this type of profile is, however, relatively easy to obtain. On the other hand, transverse profiles, given the width of the thermal trace, are more difficult to predict. In that specific respect, LES gives good agreement with the experimental database, contrary to RANS, which diffuses too much. Figure 11 also shows that the isothermal-wall

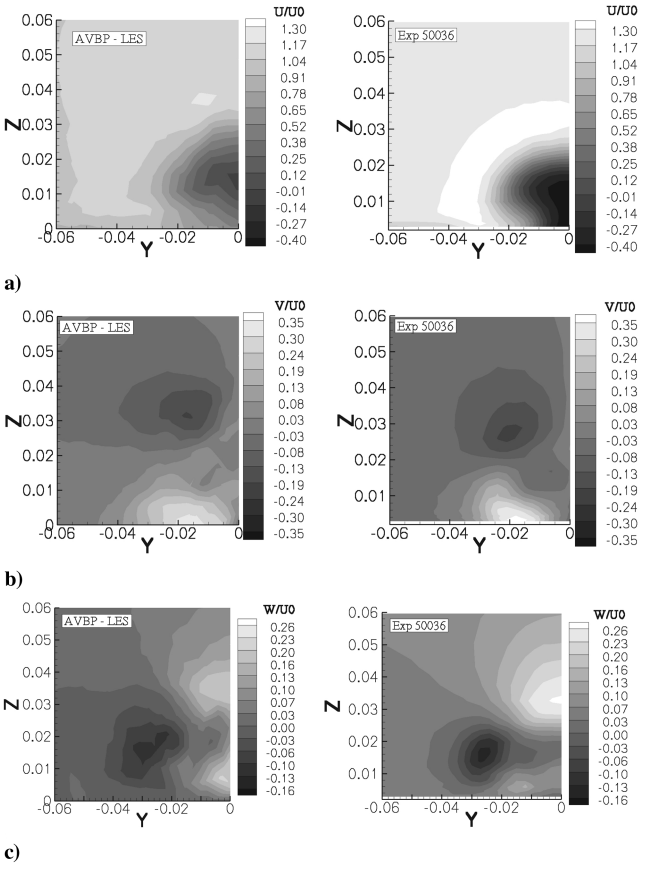

Fig. 9 Comparison of the velocity fields at $X/D = 1$ (simulation on the mesh M_1).

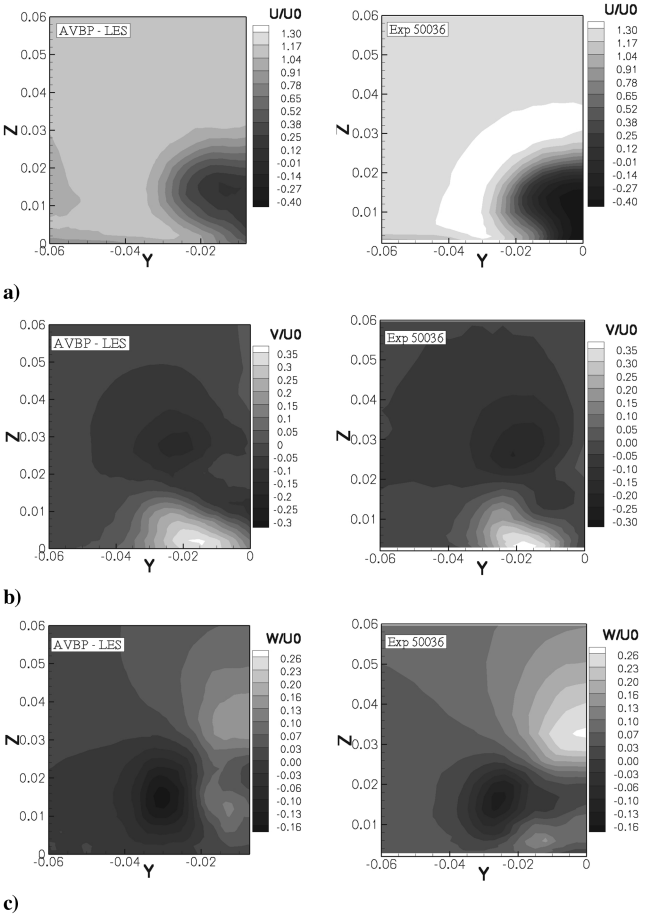

Fig. 10 Comparison of the velocity fields at $X/D = 1$ (simulation on the mesh M_2).

boundary condition applied to the grid enhances the η prediction in the $X/D = 1$ plane. The thermal transfer is better predicted with this boundary condition than with the adiabatic grid. To improve the η prediction even further, the next step would be to solve the heat transfer within the grid plate.

The velocity profiles predicted by LES (Fig. 12) do not display major differences between the coarse and fine simulations. As already mentioned for the coarse grid, the backflow region is still not well-predicted, as illustrated by the profile in the cross plane $X/D = 14$ (Fig. 12). The origin of this deficiency appears to be the wall-law treatment, which may be inadequate in this specific region. With regard to the other planes, the velocity is slightly better resolved very close to the wall.

The resolved turbulent kinetic energy (TKE) of the LES $[k = \frac{1}{2}\langle u_i' u_i' \rangle$, where $u_i' = (\tilde{u}_i - \langle \tilde{u}_i \rangle)]$ is also presented in Fig. 12 and compared with the measured data. The profiles show that the TKE is underestimated in the region next to the wall. This is explained by the fact that only the resolved scales contributing to the turbulent kinetic energy are available here, and the subgrid contribution of the LES model does not appear. In the wall region, the shear-generated small

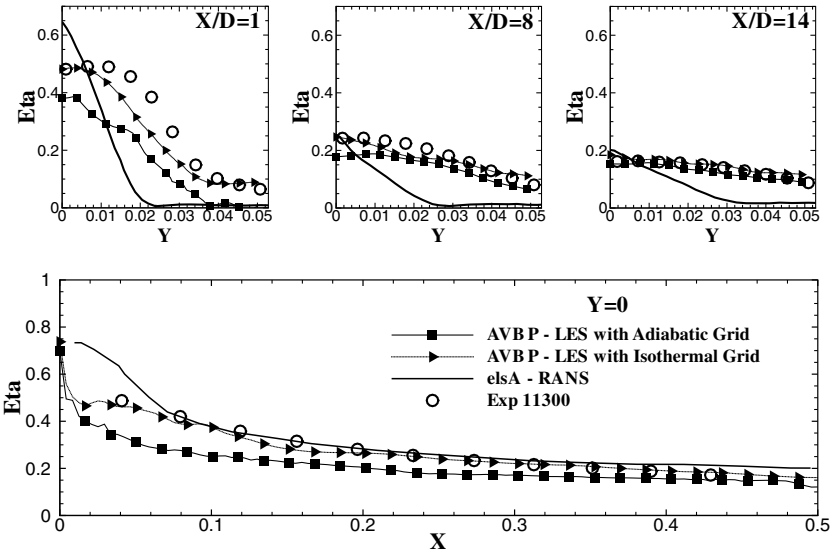

Fig. 11 Comparison of the wall-cooling-effectiveness profiles at different streamwise locations and in the spanwise symmetry plane ($Y = 0$) (simulation on mesh M_2).

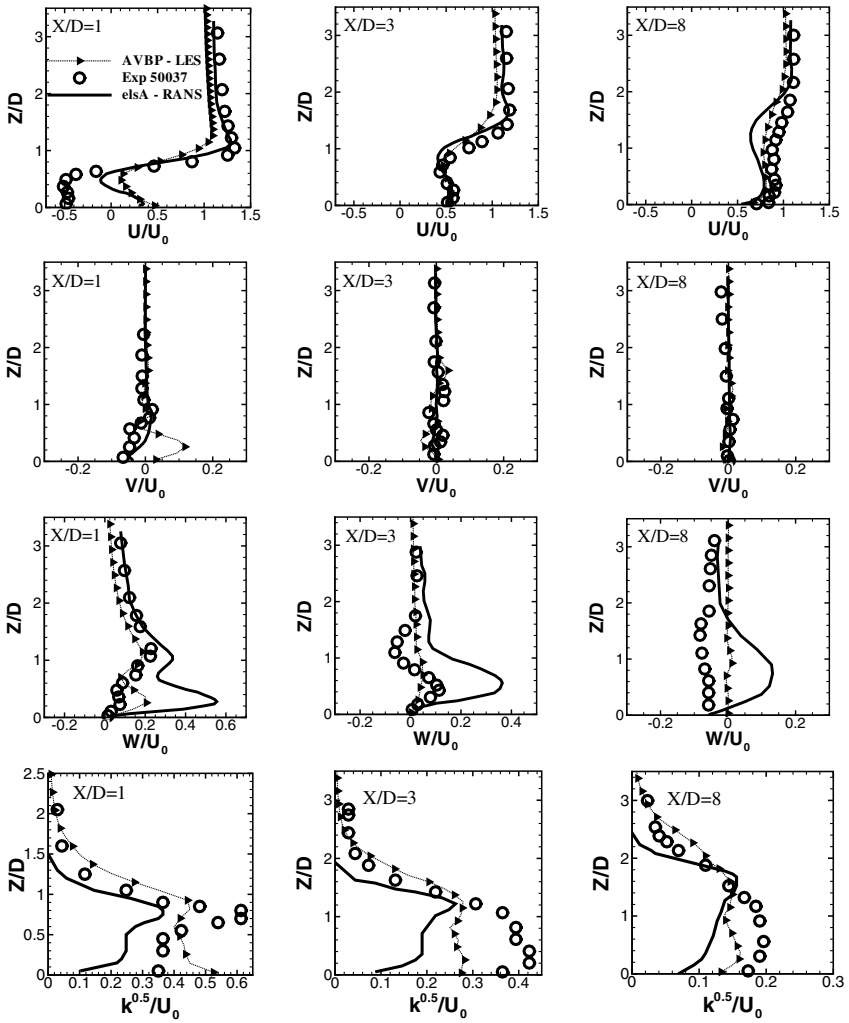

Fig. 12 Comparison of the velocity profiles and turbulent kinetic energy profiles in the symmetry plane at different streamwise locations (simulation on mesh M_2).

scales of turbulence may not be represented properly by the mesh and the wall-law model; this can also explain the underestimation. On the contrary, far away from the wall, a region dominated by very large scales, the TKE is resolved and good agreement between LES and measurements is observed. Note, however, that the standard Smagorinsky model [25] overestimates the TKE far from the wall, which is a result already observed by Schlüter and Schönfeld [34].

Instantaneous Flowfield Analysis

To illustrate the ability of LES to reproduce the interaction between the two fluids and resulting from the coherent structures, the detection criteria Q (Hunt et al. [35]) is introduced into the flow visualization. This specific diagnostic is justified by the fact that for our specific problem, in which the jet remains close to the wall, it is better than using the flow vorticity. Indeed, high vorticity marks the locations of coherent structures, but also the locations of high shear. Next to the wall, the shear is important and prevents proper identification. To cure this fault, the criteria Q is tested. The coherent structures are plotted through an isosurface in Fig. 13. An archlike coherent structure is clearly evidenced just above the jet exhaust. This pattern is observed by Andreopoulos [19] in his experimental flow visualizations and by Yuan et al. [14] in their LES.

Because of animations, one observes that this structure is shed into the main flow and positions itself above the CVP. The apparition of such a flow instability seems in agreement with the Kelvin–Helmholtz instability. Moreover, and based on the temperature as a passive scalar, it appears that the flow transported by the Kelvin–Helmholtz structures is, for the most part, issued from the scoop.

The visualization also reveals that the detachment of these structures occurs on the lateral edges of the jet exit. This phenomenon is also reported by Yuan and Street [14], who propose two mechanisms to explain the breakdown process: 1) an adverse pressure gradient on the lateral edges and 2) a strong upstream flow in the wake of the jet.

After the breakdown process, these structures composed of hot air are reoriented, stretched, and (within a short distance of roughly 6–10D) diffused by the action of the turbulent shear stresses and viscosity. Sometimes these structures impact the planar plate, leading to a crucial aerothermal process: heat is thus brought to the plate. It explains the prediction difference in the wall-cooling effectiveness obtained by RANS and LES.

Spectral Analysis

The flowfield animation and the effects of mesh refinement observed earlier reveal that capturing the coherent structures with LES is paramount to prediction of the proper mean and fluctuating

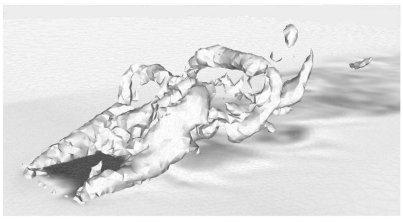

Fig. 13 Coherent structures indicated by a Q isosurface ($Q = 2.110^7$).

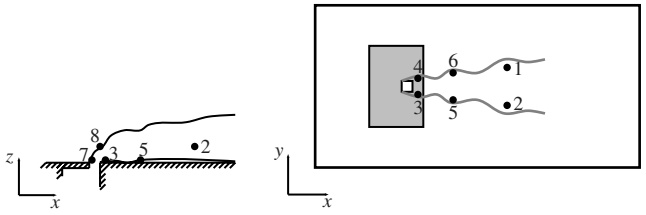

Fig. 14 Probe locations: a) wake region (top view) and b) shear-layer region (lateral view).

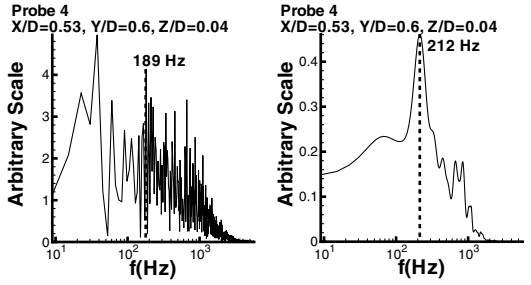

Fig. 15 Comparison between a conventional FFT approach and the Welch method.

quantities. It also explains the poor RANS predictions of the temperature profiles, because it does not simulate the unsteadiness responsible for the mixing.

To determine the role of the structures observed in Fig. 13, spectral analyses of various quantities are presented later. First, the vortex shedding behind the jet column is analyzed and observed in the LES animations. To validate the LES approach, results are compared with the experimentally measured frequencies obtained by fast Fourier transform (FFT) of the velocity signal recorded by hot-wire probes. Subsequently, after the validation of the frequency acquisition method, LES predictions are assessed against the experimental frequency measured in the shear region.

In this section, the frequency acquisition employed to study LES results is explained. Probes are located in the shear and wake regions to characterize the vortices in these areas (Fig. 14). FFTs are performed on the velocity signals using Welch's method [36]. It consists of dividing the time-series data into segments, computing a periodogram of each segment, and averaging the power spectral densities. In addition to this first step, the segments are overlapped to artificially increase the overall duration of each signal, and windows (Hanning and Blackman) are used to remove erroneous frequencies from the periodogram introduced by these manipulations (i.e., frequential resolution and dynamic resolution). Averaging is used to reduce the variance of the estimate, and overlap is introduced to decrease bias.

The parameters used for Welch's method are as follows: 0.144-s time-series duration, eight segments, Hanning or Blackman windows, and 50% overlap. To give a better view of the performance of this acquisition method, a comparison is made with a conventional FFT approach in Fig. 15. The results clearly illustrate the decrease of variance due to the Welch method and a problem that occurs when the time series are too short.

In the set of results presented later, the duration of each segment equals 0.032 s and the probes see about seven convective times, which is sufficient to trust the statistics of the periodogram. For the wake region, the spectral analysis is based on the time series of the axial-velocity component $\tilde{u}(t)$ obtained for the fine grid. For the shear region, the time series of the vertical-velocity component $\tilde{w}(t)$ are used.

Figure 16 shows the LES predictions for the probes located in the wake region downstream of the jet nozzle. LES predicts vortex shedding at a frequency corresponding to a range of Strouhal numbers $0.13 < St < 0.16$, whereas the experiment brings out a Strouhal number equal to 0.15 ($St = fD/U_0$, where D is the orifice size, U_0 is the crossflow velocity, and f is the shedding frequency). It is difficult to draw conclusions from comparisons with Strouhal numbers found in the literature, because the amount of data is limited, especially for square jets, and because the kinetic energy ratio in this study is very low ($R = 0.77$). However, it is interesting to note that Moussa et al. [7] also detected a wake Strouhal number approaching 0.15 in flows with V_R ranging from two to eight and with the Reynolds number fixed to 8000. Therefore, this study underlines the independence of the Reynolds number for the wake shedding, which confirms the work of McMahon et al. [37].

This analysis of the vortex-shedding frequency further proves the ability of LES to reproduce the flow physics. To complete the experimental database and to investigate the coherent structures illustrated in Fig. 14, the shear-layer region is investigated. In contrast with the wake, this region of the flow and, particularly, its modes are more precisely documented by other researchers. Improving the jet penetration and its spread is one of the justifications for this interest. In the present study, two probes are positioned above the upstream edge of the jet exit to characterize the structure frequency. Figure 17 shows velocity spectra in the shear-layer region of the JICF. The spectra depict a peak corresponding to a Strouhal

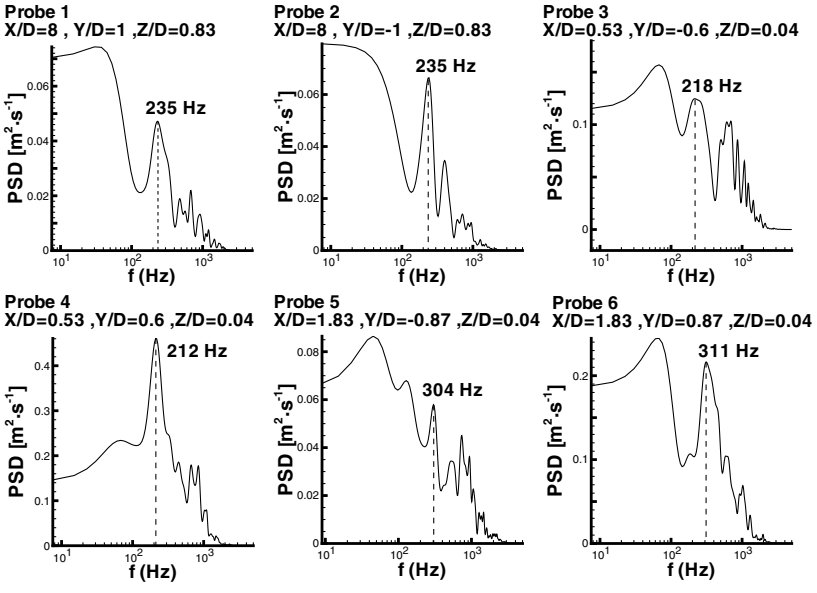

Fig. 16 Axial-velocity spectra measured at six locations downstream of the jet exit.

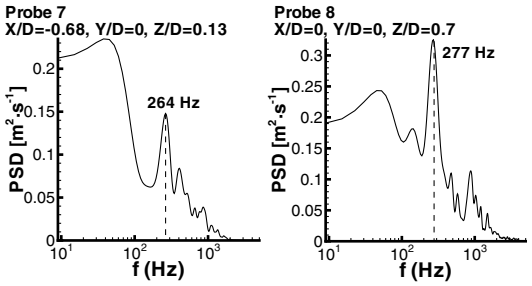

Fig. 17 Vertical-velocity spectra measured at two locations along the jet trajectory.

number equal to 0.2, and higher harmonics of the vortex roll-up frequency are observed. The spectral peak is also more distinct when the measurement is not performed close to the jet exit. This observation is confirmed by the work of Narayanan et al. [38]. However, they also noticed a decrease of the frequency value when the probe moves inside the jet, a behavior that is not observed in the present study. The results in the shear-layer region show that the coherent structure is relatively energetic. These results based on the shear-layer region confirm the importance of these coherent structures, which are important if proper mixing is to be predicted by LES.

Conclusions

Large eddy simulations are conducted to study a jet flow that is found on the leading edge of a turbofan engine nacelle, part of a work initiated by Airbus France. The aim of the study is to demonstrate the ability of this numerical method to reproduce aerothermal predictions in an industrial context. Simulations are thus conducted of a hot jet in crossflow issuing from a square nozzle, and the results are compared with those of Reynolds-averaged Navier–Stokes numerical simulations and experimental measurements. The quality of the LES predictions of cooling effectiveness are of particular interest.

The present large eddy simulations of a jet in crossflow reproduce the experimental measurements with good agreement, in contrast with Reynolds-averaged Navier–Stokes simulations. Large eddy simulation identifies several unsteady structures in the near field of the jet that are not predicted by Reynolds-averaged Navier–Stokes simulations. These structures are essential for the mixing predictions downstream of the jet, which is why particular attention must be given to the large-eddy-simulation mesh resolution.

This work also reveals that the grid's thermal boundary condition is significant, and improvements in the large-eddy-simulation predictions might require solution of the heat transfer within the grid plate. Such a task may be considered for future developments, because coupling a computational fluid dynamics solver with a thermal code is conceivable with computational frameworks such as PALM , for example.

Finally, spectral analyses of the wake and shear-layer regions demonstrate the quality of the large-eddy-simulation predictions obtained here and further illuminate the unsteady flow features. However, and as of today, current large-eddy-simulation applications remain limited from an aerothermal point of view, because of the very high Reynolds number usually involved (about $Re = 60 \times 10^6$). Nonetheless, this work proves the potential of large eddy simulation for this type of problem, with important industrial implications.

Acknowledgment

The authors gratefully acknowledge Airbus France for its support.

References

[1] Margason, R. J., "Fifty Years of Jet in Crossflow Research," *Computational and Experimental Assessment of Jets in Crossflow*, CP-534, AGARD, Neuilly sur Seine, France, 1993, p. 1.1–1.41.

[2] Albugues, L., "Analyse Expérimentale et Numérique d'un Jet Débouchant dans un Ecoulement Transverse," Ph.D. Thesis, École Nationale Supérieure de l'Aéronautique et de l'Espace, Toulouse, France, 2005.

[3] Prière, C., Gicquel, L. Y. M., Kaufmann, A., Krebs, W., and Poinsot, T., "LES of Mixing Enhancement: LES Predictions of Mixing Enhancement for Jets in Cross-Flows," *Journal of Turbulence*, Vol. 5, 2004, p. 5.

[4] Prière, C., Gicquel, L. Y. M., Gajan, P., Strzelecki, A., Poinsot, T., and Bérat, C., "Experimental and Numerical Studies of Dilution Systems for Low Emission Combustors," *AIAA Journal*, Vol. 43, No. 8, 2005, pp. 1753–1766.

[5] Kamotani, Y., and Greber, I., "Experiments on a Turbulent Jet in Crossflow," *AIAA Journal*, Vol. 10, No. 11, 1972, pp. 1425–1429.

[6] Fearn, R. L., and Weston, R. P., "Induced Velocity Field of a Jet in a Crossflow," NASA TP-1087, 1978.

[7] Moussa, Z. M., Trischka, J. W., and Eskinazi, S., "The Near Field in the Mixing of a Round Jet with a Cross-Stream," *Journal of Fluid Mechanics*, Vol. 80, Apr. 1977, pp. 49–80.

[8] Andreopoulos, J., and Rodi, W., "Experimental Investigation of Jets in a Crossflow," *Journal of Fluid Mechanics*, Vol. 138, 1984, pp. 93–127.

[9] Perry, A. E., Kelso, R. M., and Lim, T. T., "Topological Structure of a Jet in a Crossflow," *Computational and Experimental Assessment of Jets in Cross Flow* , CP-534, AGARD, Neuilly sur Seine, France, 1993, pp. 12.1–12.8.

[10] Coelho, S. L. V., and Hunt, J. C. R., "The Dynamics of the Near Field of Strong Jets in Crossflows," *Journal of Fluid Mechanics*, Vol. 200, Mar. 1989, pp. 95–120.

[11] Cortelezzi, L., and Karagozian, A. R., "On the Formation of the Counter-Rotating Vortex Pair in Transverse Jets," *Journal of Fluid Mechanics*, Vol. 446, Nov. 2001, pp. 347–373.

[12] Krothapalli, A., Lourenco, L., and Buchlin, J. M., "Separated Flow Upstream of a Jet in a Crossflow," *AIAA Journal*, Vol. 28, Mar. 1990, pp. 414–420.

[13] Kelso, R. M., Lim, T. T., and Perry, A. E., "An Experimental Study of Round Jets in Cross-Flow," *Journal of Fluid Mechanics*, Vol. 306, 1996, pp. 111–144.

[14] Yuan, L. L., Street, R. L., and Ferziger, J. H., "Large Eddy Simulations of a Round Jet in Crossflow," *Journal of Fluid Mechanics*, Vol. 379, 1999, pp. 71–104.

[15] Smith, S. H., and Mungal, M. G., "Mixing, Structure and Scaling of the Jet," *Journal of Fluid Mechanics*, Vol. 357, No. 1, Feb. 1998, pp. 82–122.

[16] Fric, T. F., and Roshko, A., "Vortical Structure in the Wake of a Transverse Jet," *Journal of Fluid Mechanics*, Vol. 279, 1994, pp. 1–47.

[17] Callaghan, E. E., and Rugger, R. S., "Investigation of the Penetration of an Air Jet Directed Perpendicularly to an Air Stream," NASA TN 1615, 1948.

[18] Williams, J., and Wood, M. N., "Aerodynamic Interference Effects with Jet Lift Schemes on VSTOL Aircraft at Forward Speeds," AGARD Rept. AG-103, 1965, pp. 625–651.

[19] Andreopoulos, J., "On the Structure of Jets in a Crossflow," *Journal of Fluid Mechanics*, Vol. 157, Aug. 1985, pp. 163–197.

[20] Renze, P., Meinke, M., and Schröder, W., "LES of Turbulent Mixing in Film Cooling Flows," *Conference on Turbulence and Interactions (TI2006)* [CD-ROM], ONERA, Toulouse, France, June 2006; also available at http://www.onera.fr/congres/ti2006/definitivepapers/Renze.pdf [retrieved 8 August 2007].

[21] Favre, A., "Statistical Equations for Turbulent Gases," *Problems of Hydrodynamics and Continuum Mechanics*, Society for Industrial and Applied Mathematics, Philadelphia, PA, 1969, pp. 231–266.

[22] Sagaut, P., "Large Eddy Simulation for Incompressible Flows," *An Introduction*, 2nd ed., Springer–Verlag, New York, 2002.

[23] Poinsot, T., and Veynante, D., *Theoretical and Numerical Combustion*, 2nd ed., R. T. Edwards, Philadelphia, 2005.

[24] Rogallo, R. S., and Moin, P., "Numerical Simulation of Turbulent Flows," *Annual Review of Fluid Mechanics*, Vol. 16, 1984, pp. 99–137.

[25] Smagorinsky, J., "General Recirculation Experiments with the Primitive Equations, 1: The Basic Experiment," *Monthly Weather Review*, Vol. 91, No. 3, 1963, pp. 99–164.

[26] Martin, C. E., Benoit, L., Sommerer, Y., Nicoud, F., and Poinsot, T., "Large-Eddy Simulation and Acoustic Analysis of a Swirled Staged Turbulent Combustor," *AIAA Journal*, Vol. 44, No. 4, 2006, pp. 741–750.

[27] Schmitt, P., Poinsot, T., Schuermans, B., and Geigle, K., "Large-Eddy Simulation and Experimental Study of Heat Transfer, Nitric Oxide Emissions and Combustion Instability in a Swirled Turbulent High Pressure Burner," *Journal of Fluid Mechanics*, Vol. 570, 2007, pp. 17–46.

[28] Dandois, J., and Garnier, E., "Unsteady Simulation of a Synthetic Jet in a Crossflow," *AIAA Journal*, Vol. 44, No. 2, 2006, pp. 225–238.
[29] Rizetta, D. P., Visbal, M. R., and Stanek, M. J., "Numerical Investigation of Synthetic-Jet Flowfields," *AIAA Journal*, Vol. 37, No. 8, 1999, pp. 919–926.
[30] Poinsot, T., and Lele, S. K., "Boundary Conditions for Direct Simulations of Compressible Viscous Flows," *Journal of Computational Physics*, Vol. 101, No. 1, July 1992, pp. 104–129.
[31] Thompson, K. W., "Time Dependent Boundary Conditions for Hyperbolic Systems," *Journal of Computational Physics*, Vol. 68, Jan. 1987, pp. 1–24.
[32] Selle, L., Nicoud, F., and Poinsot, T., "The Actual Impedance of Non-Reflecting Boundary Conditions: Implications for the Computations of Resonators," *AIAA Journal*, Vol. 42, No. 5, 2004, pp. 1–21.
[33] Cambier, L., and Gazaix, M., "elsA: An Efficient Object-Oriented Solution to CFD Complexity," 40th AIAA Aerospace Science Meeting and Exhibit, Reno, NV, AIAA Paper 2002-0108, 2002.
[34] Schlüter, J. U., and Schönfeld, T., "LES of Jets in Crossflow and its Application to Gas Turbine Burners," *Flow, Turbulence and Combustion*, Vol. 65, No. 2, 2000, pp. 177–203.
[35] Hunt, J. C. R., Wray, A. A., and Moin, P., "Eddies, Streams; and Convergence Zones in Turbulent Flows," *Studying Turbulence Using Numerical Simulation Databases–7*, NASA Ames Research Center, Moffett Field, CA, 1988.
[36] Welch, P. D., "The Use of Fast Fourier Transform for the Estimation of Power Spectra: A Method Based on Time Averaging over Short, Modified Periodograms," *IEEE Transactions on Audio and Electroacoustics*, Vol. AU-15, No. 2, 1967, pp. 70–73.
[37] McMahon, H. M., Hester, D. D., and Palfery, J. G., "Vortex Shedding from a Turbulent Jet in a Cross-Wind," *Journal of Fluid Mechanics*, Vol. 48, No. 1, July 1971, pp. 73–80.
[38] Narayanan, S., Barooah, P., and Cohen, J. M., "Dynamics and Control of an Isolated Jet in Crossflow," *AIAA Journal*, Vol. 41, No. 12, 2003, pp. 2316–2330.
[39] Buis, S., Piacentini, A., and Déclat, D., "PALM: A Computational Framework for Assembling High Performance Computing Applications," *Concurrency and Computation: Practice & Experience*, Vol. 18, No. 2, 2006, pp. 231–245.

P. Givi
Associate Editor